RESEARCH PAPER

MicroPIV and micromixing study of corona wind induced microcentrifugation flows in a cylindrical cavity

Jiaxing J. Qin · Leslie Y. Yeo · James R. Friend

Abstract Recently, a novel way of driving rapid microcentrifugation was discovered using ionic wind via ionization of the atmosphere around a singular electrode tip, driving liquid recirculation in a small cylindrical cavity due to interfacial shear. In the original work, the primary azimuthal surface recirculation was speculated to drive a secondary flow in the bulk of the liquid which resembles a helical swirling flow that tapers toward a pseudo-stagnation point at the cavity floor, analogous to Batchelor flows between co-axially placed stationary and rotating disks. Here, we employ microParticle Image Velocimetry (microPIV) together with numerical simulations to verify this speculation. Good qualitative and reasonable quantitative agreements were obtained between the experiments and numerical simulations. In both, we were able to capture salient features of the three-dimensional flow; for the experiments, this was achieved by the reconstruction of the three-dimensional flow field from the planar two-dimensional velocity fields obtained in a confocal-like manner. In addition, we formally quantify the micromixing enhancement first demonstrated, but not quantified, in the original experiments. Our results show a mixing enhancement close to two orders of magnitude approaching vigorous mixing intensities as the surface vortices suffer from various instabilities leading towards their breakdown into subvortices at large applied voltages and AC frequencies, reminiscent of that in the original work.

1 Introduction

Fluid transport at the micro- and nanoscale is in many senses regulated by the characteristic ratio of the fluid surface area to its volume. The inverse scaling of this characteristic ratio imposes a large value at small scales associated with micro- and nanofluidics. At these small scales, surface forces (such as viscous and capillary stresses), which tend to retard fluid motion, dominate over body forces (such as inertial, gravitational or induced acceleration forces), which can generally be exploited to induce fluid motion. The surface area to volume ratio therefore directly indicates the difficulty one will encounter in inducing fluidic motion, and thus the challenge of working with fluids at small scales. Considerable progress has been made in the development of micropumps (Laser and Santiago 2004), with the most promising technology being electroosmotic pumps (Chen and Santiago 2002; Li 2004; Wang et al. 2006), or more recently, surface acoustic wave pumps (Tan et al. 2007; Yeo and Friend 2009).

In many researchers' concerted efforts to develop micromixers, microvalves and microseparators, microcentrifugation (Ducree 2008) appears to be an ignored afterthought (Nguyen and Wereley 2006). This is perhaps due to the difficulty in generating sufficient centrifugal forces at small scales to overcome the fluid resistance, as discussed above. Over 10 years ago, microfluidic channels and

J. J. Qin · L. Y. Yeo (✉) · J. R. Friend
Micro/Nanophysics Research Laboratory, Monash University, Clayton, VIC 3800, Australia
e-mail: leslie.yeo@eng.monash.edu.au

J. J. Qin
e-mail: Jiaxing.Qin@eng.monash.edu.au

J. R. Friend
e-mail: James.Friend@eng.monash.edu.au

components were fabricated on a disk similar in size to a compact disk (CD), and by rotating the entire disk, small-scale centrifugation was generated through Coriolis forces (Madou et al. 2006). This concept has recently been exploited to separate plasma from whole blood (Guigan 1998; Pugia et al. 2004; Haeberle et al. 2006). However, the high speed rotation of the entire disk structure in order to generate sufficient centrifugation is not just confined to the fluid that is to be centrifuged, as the upstream or downstream components to the reactor and separator are exposed to the same centripetal acceleration. This is a severe limitation as the rotation can cause undesirable effects in the upstream or downstream components such as the dispenser and detector, and the integration of the rotational structure with other stationary components can be extremely difficult. In addition, the machine which generates the rotation is large and cumbersome, quite the antithesis of microfluidic philosophy, of which the ultimate goal is the integration of all fluid processing components onto a single chip-sized device. In a separate work, flow separation in the opening of a smooth channel's side cavity was exploited to generate microvortices within the cavity, achieving some degree of vorticity (Shelby et al. 2003). However, the fabrication of these side cavities into microchannels may not always be convenient and not all particles suspended in the liquid enter the cavity from the main channel, thus posing a limitation on the particle separation efficiency.

More recently, we reported a novel way to drive microcentrifugation by employing a sharp pin electrode mounted with a small air gap above a cylindrical cavity in which the liquid is housed, as depicted in Fig. 1 (Yeo et al. 2006a, b; Arifin et al. 2007). When a voltage exceeding a certain threshold is applied, atmospheric ionization ensues (Loeb 1965). Ions of the same polarity to the electrode tip are then repelled, colliding into neutral air molecules in the process. This transfer of momentum generates a strong

airflow known as *ionic wind* (see Fig. 1). By directing the electrode and hence the airflow towards a liquid surface, the surface itself is sheared, hence generating fluid recirculation on the surface and consequently in the bulk of the liquid. If the electrode is mounted vertically and symmetrically centered above the liquid surface (Fig. 2a), the radial outward air flow then results in an axisymmetric shear at the liquid surface. Due to flow conservation, the radially outflowing liquid must then recirculate, resulting in internal recirculation vortices in the bulk of the liquid (Ohyama et al. 2003). If the electrode is inclined (Fig. 2b, c); however, different primary flow behaviors arise. A pair of surface vortices is produced if the electrode is placed symmetrically along the centerline, as depicted in Fig. 2b. If the electrode is placed laterally, a single surface vortex is generated, as depicted in Fig. 2c. The latter flow behavior thus constituted the first concept of a microcentrifuge that does not require the bulk rotation of the entire fluidic chamber or any other mechanically moving parts, and was demonstrated as an effective micromixer as well as a mechanism to separate or concentrate particles (Yeo et al. 2006b)—for example, the separation of red blood cells from blood plasma (Yeo et al. 2006a; Arifin et al. 2007).

The mechanism that gives rise to the bulk helical flow associated with the configuration shown in Fig. 2c was speculated in Yeo et al. (2006a) and Arifin et al. (2007). Briefly, the primary azimuthal recirculation at the surface of the liquid due to the ionic wind shear drives a secondary meridional recirculation in the bulk. However, the stationary base of the cavity floor imposes a no-slip condition that retards the azimuthal rotation and hence suppresses the centrifugal force towards the cavity bottom (Fig. 3) such that a helical swirling flow is generated in the bulk in a similar manner to *Batchelor flows* that arise in the interstitial fluid between a stationary and rotating disk (Batchelor 1951; Pao 1972).
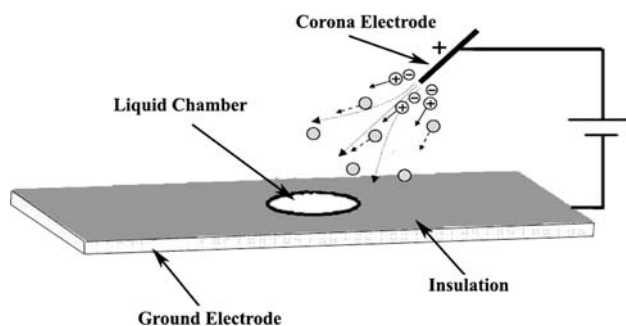

Fig. 1 Schematic representation of the microcentrifugation device. The air flow arises due to the ionic wind mechanism depicted in the figure when the sharp electrode tip is raised to a voltage beyond the threshold ionization potential. The liquid contained in the cylindrical cavity is driven to recirculate by directing this air flow towards its surface
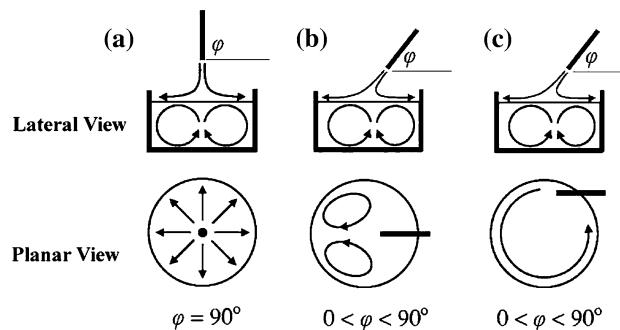

Fig. 2 Depending on the orientation and position of the corona electrode, various liquid recirculation patterns can arise, as shown by the schematic illustrations. The bulk liquid recirculation is a secondary phenomenon accompanying the primary surface recirculation
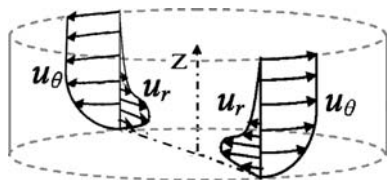
Fig. 3 Azimuthal (u_θ) and radial (u_r) velocity profiles showing how recirculation arises due to the decrease in the azimuthal velocity and hence centrifugal force, and the associated increase in the inward radial velocity within the *Ekman layer* as a consequence

In this paper, we verify the speculated mechanism through experimental flow field visualization using microParticle Image Velocimetry (microPIV) (Papautsky et al. 2008) and numerical flow simulations. Both results form good agreement with each other and with the speculated behavior, thus confirming the hypothesis of our earlier work (Yeo et al. 2006a; Arifin et al. 2007). In addition, the possibility that the microcentrifugation technique can be exploited for micromixing was qualitatively demonstrated in Yeo et al. (2006b). However, a quantification of the mixing efficiency was not provided—an additional component of this work is therefore to formally quantify the enhancement in the mixing intensity using a pixel intensity analysis.

We proceed by describing the experimental setup and the process by which we reconstruct a three-dimensional flow field from confocal-like two-dimensional planar microscopic flow imaging and the method by which the pixel intensity analysis is carried out to quantify the mixing

action. This is followed by a description of the computational flow dynamics scheme to simulate the three-dimensional flow field. Consequently, we discuss the results from the microPIV experiments, numerical simulations and the micromixing analysis, and finally conclude with a summary of our findings.

2 Experimental setup

2.1 Microcentrifugation

A schematic of the experimental setup is shown in Fig. 4. The corona electrode, which consisted of a sharp tungsten pin, was connected to a high voltage transformer (4100, EMCO, Sutter Creek, CA) with output voltage ranging from 1 to 10 kV, providing a steady DC voltage to the electrode. The transformer was powered by a high speed bipolar amplifier (BA4825, NF Corporation, Yokohama, Japan) and the voltage variation was controlled by a multifunction synthesizer (WF 1966, NF Corporation, Yokohama, Japan). The cylindrical cavity was fabricated by punching a 4 mm diameter hole through a 2 mm thick rubber sheet, which was then glued onto a glass microscope slide coated with indium tin oxide (ITO, SPI Labs, 3 Ω resistance, Palo Alto, CA), thereby constituting the ground electrode. The transparency of the ITO facilitates visualization of the flow within the cavity from below using an inverted fluorescent microscope (IX71, Olympus, Tokyo, Japan) connected to a high-speed camera (HiSense MkII,

Fig. 4 Schematic representation of the experimental setup used to generate the electrohydrodynamic air thrust, and hence, the rotational liquid flow. The *inset* shows the position of the corona electrode
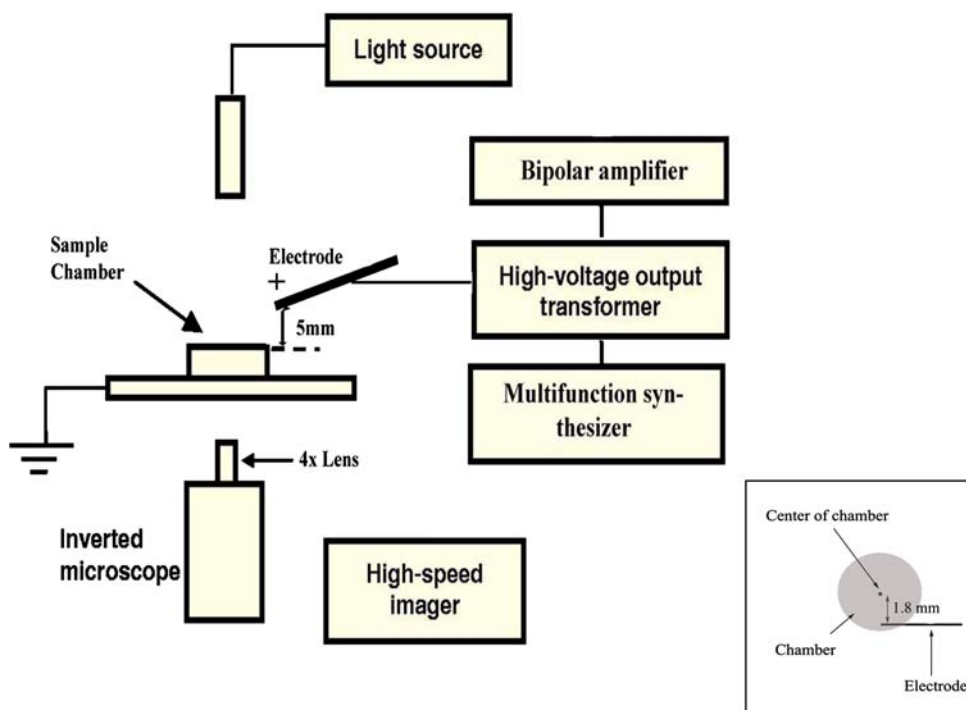
Dantec Dynamics, Skovlunde, Denmark) capable of imaging up to 5,000 frames/s.

The working fluid consisted of deionized water, seeded with 8 μm fluorescent polystyrene particles (36-3, Duke Scientific, Fremont, CA) with absorption and emission maxima at 542 and 612 nm, respectively. The corona electrode was mounted 5 mm above the fluid surface at an angle around 10° from horizontal to generate sufficient interfacial shear to drive the recirculation. To obtain the azimuthal surface recirculation shown in Fig. 2c, the corona electrode was placed at the edge of the chamber, off-centered by 1.8 mm, as depicted in the schematic. In these experiments, the applied DC voltage was held constant at 2.1 kV to obtain a steady laminar flow. It should be mentioned that we employed a higher voltage to drive sufficiently large bulk liquid recirculation velocities than that used in the blood plasma separation experiments (Yeo et al. 2006a; Arifin et al. 2007) to avoid the seeded microparticles from being trapped at the bottom stagnation point; resuspension of the particles back into the bulk occurs if the convective velocity is larger than the sedimentation velocity of the particles (Arifin et al. 2007).

The particle-laden flow field was illuminated through a 532 nm laser (Solo PIV, New Wave, Fremont, CA) with an output energy of 15 mJ and repetition rate of 15 Hz, coupled via a fibre optic cable to the microscope with 4× magnification objectives, which has a focal depth of approximately ±10 μm. The laser focal plane was varied from the bottom of the cavity upwards by 100 μm increments up to a height of 1 mm in order to obtain confocal-like two-dimensional planar cross-sectional images of the flow field (Raghavan et al. 2009).

The fluid velocities in the (x,y) directions, u and v, respectively, were subsequently acquired by tracking the particle trajectories (FlowManager, Dantec Dynamics, Skovlunde, Denmark), using an adaptive correlation with an interrogation area of 64 × 64 pixels and 25% overlap. The experimental data was acquired in cartesian coordinates and later converted to cylindrical coordinates. The vertical (z) velocities w can then be computed through the steady, incompressible, continuity equation (Eq. 1) (Kinoshita and Kaneda 2007).

$$\frac{\partial u}{\partial x} + \frac{\partial v}{\partial y} + \frac{\partial w}{\partial z} = 0. \tag{1}$$

2.2 Micromixing

To analyse the mixing intensity, we pipetted a small amount of red commercial food colouring without pretreatment onto the surface of the working fluid, taking care to ensure that the injection pressure or the inertial impact on the liquid surface due to the addition of the dye did not result in convective spreading. The electric field was then applied immediately to drive the surface recirculation and the evolution of the dye as it mixed with the rest of the fluid, while the process was tracked via a high speed microscopic flow imaging system described above. In these experiments, we employed alternating current (AC) electric fields to observe the effect of the frequency on the enhancement in the mixing. The AC field was generated using a function/arbitrary waveform generator (32220A, Agilent Technologies, Santa Clara, CA) connected to a high voltage output transformer (113459-1, 10–70 kHz, Industrial Test Equipment, Port Washington, NY) and an amplifier (Powetron 250 A, 10 Hz to 1 MHz, Industrial Test Equipment, Port Washington, NY) capable of delivering up to 6,000 V (peak-to-peak) and 250 W. The images were captured at 60 frames/s using a high speed camera (Olympus iSpeed) connected to the inverted microscope with a 4× magnification lens. Details of the pixel intensity analysis will be provided subsequently.

3 Numerical simulation

To model the fluid flow within the cylindrical cavity, we assumed that the rotational motion of the liquid surface induced by the ionic wind thrust is similar to the motion of a rotational disk. We neglect any free surface deformation, which is not an unreasonable assumption given that the shallow inclination of the corona electrode (less than 10°) does not lead to sufficient normal stresses imparted on the free surface by the air flow (Kawamoto and Umezu 2005) as compared to the large shear imposed by the tangential shear stress that generates the fluid rotation in the cavity. Consequently, we model the liquid free surface as a rigid surface (Raghavan et al. 2009). This simplifies the model considerably since the gas phase electrohydrodynamics are decoupled from the liquid phase hydrodynamics, and hence only the latter needs to be solved. The driving force of the liquid flow due to the ionic wind thrust then only enters the system as a boundary condition imposed on the liquid surface. This approach can be justified as the relative permittivity of the liquid (typically 78 for water) is much greater than that for air (typically 1), which allows us to assume that the surface charges at the air–water interface can be neglected, i.e., $q_s \approx 0$, due to weak polarization of the liquid and the tendency of the gas phase ions to accumulate at the near singular sharp tip of the corona electrode. The interfacial jump conditions (Eqs. 2, 3) then stipulate that the normal electric field (E_n) in the liquid phase (l) is negligible compared to that in the gas phase (g). Essentially, the liquid behaves as a conducting electrode with constant potential and hence the possibilities of any liquid motion induced by an existing electric field may be omitted, and so the convective liquid flow is caused only

by the ionic wind shear imposed on the liquid surface. The electric field boundary conditions are

$$[E_t]_l^g = 0, \tag{2}$$

$$[\epsilon E_n]_l^g = q_s; \tag{3}$$

where E_t denotes the tangential electric field. The square parentheses in the above denote the jump in the inner quantity across the interface. In addition, we note that the absence of field gradients in the liquid phase also suggests that the effect of dielectrophoretic forces on the particle mobility is negligible when comparing the apparent velocity observed in the experiments with the velocity obtained from the numerical prediction. For incompressible steady flow, the dynamics of the motion of the liquid in the cylindrical cavity are governed by the incompressible continuity and Navier–Stokes equations

$$\nabla \cdot \mathbf{U} = 0 \tag{4}$$

and

$$\rho \frac{\partial \mathbf{U}}{\partial t} + \rho \mathbf{U} \cdot \nabla \mathbf{U} = -\nabla p + \nabla \cdot \boldsymbol{\tau}, \tag{5}$$

respectively, wherein the stress tensor $\boldsymbol{\tau}$ is related to the strain rate through

$$\boldsymbol{\tau} = \mu(\nabla \mathbf{U} + (\nabla \mathbf{U})^T). \tag{6}$$

Above, ρ is the density, μ the viscosity, $\mathbf{U}$ the velocity field, p the pressure and t the time; the superscript T implies the transpose of the inner quantity in the parenthesis. We henceforth adopt cylindrical coordinates (r, θ, z) to describe the problem. No-slip boundary conditions were imposed at the stationary side walls and floor of the cavity:

$$\mathbf{U} = 0 \quad \text{at } r = 2\,\text{mm}, \ z \le 2\,\text{mm} \text{ and } r \le 2\,\text{mm}, z = 0, \tag{7}$$

whereas the following boundary condition is imposed at the free surface of the liquid:

$$[u_r, u_\theta, u_z] = F(r, z) \quad \text{at } r \le 2\,\text{mm}, \ z = 2\,\text{mm}, \tag{8}$$

where $F(r, z)$ represents the velocity profile at the free liquid surface obtained experimentally (Fig. 5b). We present here a simple scaling argument for the velocity at the liquid surface, which we use as an order-of-magnitude check of the experimentally determined values. For steady inviscid flow in the absence of an imposed pressure gradient, the hydrodynamic equation governing momentum conservation (Eq. 5) in the gas phase reduces to

$$\rho_g \mathbf{U}_g \cdot \nabla \mathbf{U}_g = \rho_e \mathbf{E}_g, \tag{9}$$

where ρ_g is the density and $\mathbf{U}_g$ the velocity vector of the gas phase. ρ_e is the charge density and $\mathbf{E}_g = -\nabla \phi_g$ is the gas phase electric field in which ϕ_g is the electric potential. The charge density is given by the Poisson equation

$$\rho_e = -\epsilon_0 \nabla^2 \phi_g, \tag{10}$$

where ϵ_0 is the permittivity of free space. We thus obtain an estimate for the gas phase velocity by a dominant balance between the inertial and Columbic forces:

$$U_g \sim \left(\frac{\epsilon_0}{\rho_g}\right)^{\frac{1}{2}} \frac{V}{L_e}, \tag{11}$$

where $V \sim 10^3$ V is the applied voltage and $L_e \sim 10^{-3}$ m is the separation between the electrode and the liquid interface, suggesting that $U_g \sim 1$ m/s. Applying continuity of tangential stresses at the interface, the resulting liquid velocity at the surface can then be estimated:

$$U_l \sim \frac{\mu_g}{\mu_l} \frac{H}{L_e} U_g, \tag{12}$$

where μ_g and μ_l are the gaseous and liquid phase viscosities, respectively, and $H \sim 10^{-3}$ m is the depth of the cylindrical chamber. Equations (11) and (12) then stipulate that the liquid surface linear velocities U_l are on the order of 1 mm/s, in agreement with experiments (0.3–3 mm/s).

Fig. 5 a Experimental flow velocity field obtained at liquid heights $z = 1$ mm, 0.8 m and 0.5 mm. **b** The three-dimensional velocity field at $z = 1$ mm, constructed from **a** by applying Eq. 1. The values of the velocity field were then applied as the boundary condition of the free liquid surface
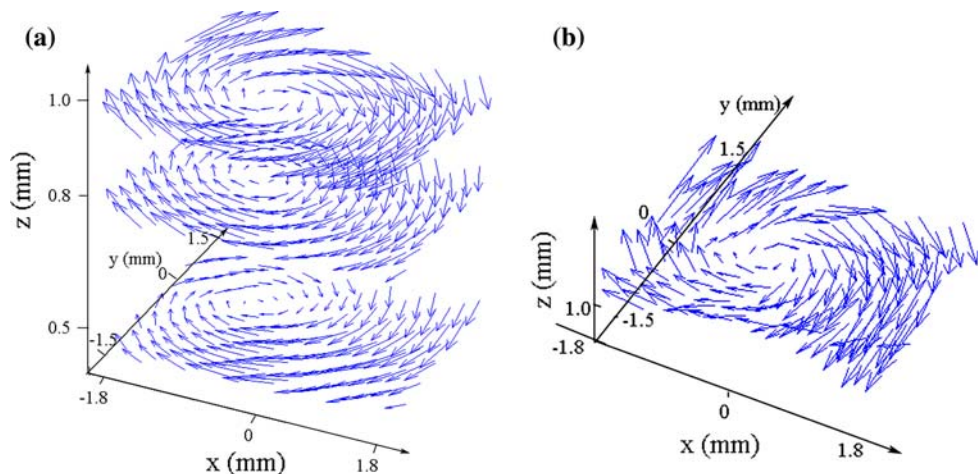
The typical bulk Reynolds number in the experiments is of order 1, implying that the non-linear and viscous terms of Eq. (5) are comparable. As a result, the steady and laminar incompressible form of Eqs. (4) and (5) are solved subject to the no-slip and rotational boundary conditions given above for the cylindrical geometry of the cavity. The dimensions of the cavity are stipulated by the experimental setup employed using a finite element solver Ansys CFX (Workbench CFX 11.0, Ansys Inc., Canonsburg, PA), with 901,773 three-dimensional brick elements to define the volume, shape functions for the pressure gradient and diffusion terms, and a first order upwind difference scheme for the advective term. The mesh density was progressively refined in steps until convergence based on the error norm occurred without fail and the reported results were identical across the three most refined mesh densities. A first order backward Eulerian implicit solution scheme was used as a coupled solver to determine the spatial distribution of the flow velocities $\mathbf{U}$ and pressure p using an adaptive time step to arrive at a converged steady-state solution in a physically based manner. The scheme uses a multigrid accelerated incomplete lower upper (ILU) factorization technique to solve the discretized equations (Hutchinson and Raithby 1986; Raw 1996). The working fluid was chosen to be water at 25°C and 1 atm pressure with a

dynamic viscosity and density of 8×10^{-4} kg/ms and 997 kg/m^3, respectively.

4 Results and discussion

4.1 Three-dimensional flow reconstruction and comparison with numerical simulations

Figure 6 compares the transverse velocity magnitude distribution $|\mathbf{U}|$ of the experiments and numerical solutions. The reasonable agreement between both experiment and numerical simulation results confirms earlier speculations (Yeo et al. 2006a; Arifin et al. 2007) that the primary azimuthal surface recirculation driven by the ionic wind gives rise to a secondary bulk meridional recirculation, as illustrated in Fig. 2c. Figure 7 on the other hand, shows the vertical (z) velocity in the y–z plane obtained through the numerical simulations from which we observe the steady downward flow along the side walls of the cavity, and the return of the fluid to the top part of the cavity through the central column where the center of the vortex is located. To aid visualization, we have reconstructed in Fig. 8 a three-dimensional flow field trace from the numerical results that shows the liquid being drawn circumferentially downwards
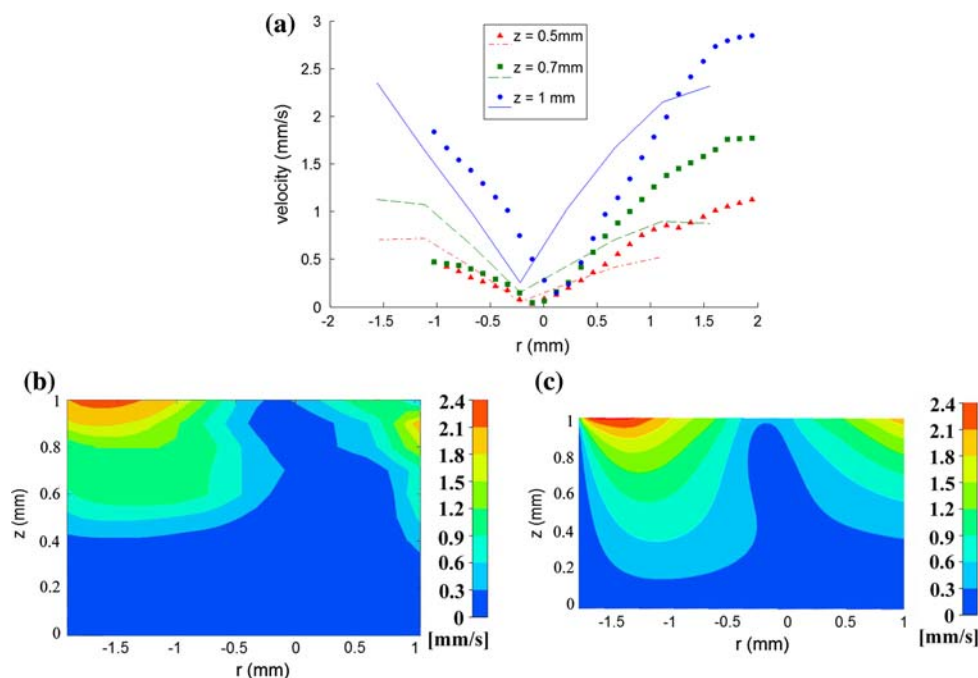

Fig. 6 a Velocity $|\mathbf{U}| = \sqrt{u_r^2 + u_z^2 + u_\theta^2}$ as a function of radial position at various depths in the cylindrical cavity, inferred from both the experimental (*points*) flow field data and the numerical (*lines*) simulations. The slight offset of the vortex center from $r = 0$ is due to the offset in the positioning of the corona electrode. **b** An experimental velocity $|\mathbf{U}|$ contour plot in the y–z plane obtained

through a reconstruction of the two-dimensional planar velocity flow fields observed using microPIV at various depths, and **c** a numerically determined contour plot of the same quantity for comparison. In both **b** and **c**, we observe the velocity to decrease toward the stationary sidewalls, the floor of the cavity and the cavity center where the velocity is zero due to the central vortex
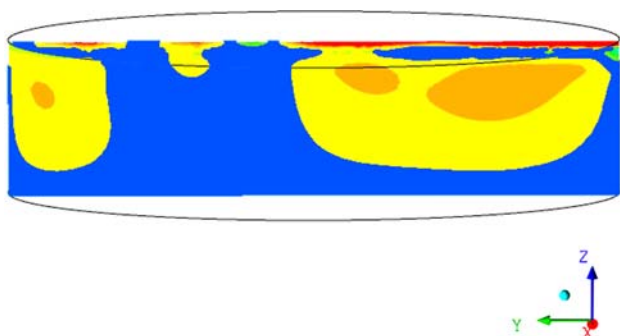
Fig. 7 Vertical (z) velocity contours in the y–z plane; warm (*bright*) colours (*orange* and *yellow*) indicate downward motion against the respective axis directions, while cool (*dark*) colours (*blue*) indicates upward motion along the axis direction

along the sidewalls of the cavity before returning upwards via a central column. The asymmetry of the flow fields in Figs. 6, 7 and 8 about the vertical axis (slightly offset from the central axis $r = 0$) arises due to the inclination of the needle and its position to one side of the circular cavity (Fig. 2c).

In both experiment (Fig. 6b) and numerical simulation (Fig. 6c), we observe the formation of a helical vortex structure. It is this helical vortical structure that is responsible for the spiralling of the particles and hence their agglomeration at a bottom stagnation point employed for the separation of red blood cells from blood plasma in previous works (Yeo et al. 2006a; Arifin et al. 2007).

From the velocity distribution in Fig. 6, we can estimate the characteristic size of the vortex as a function of the vertical position of the liquid from the chamber floor. This can be done by computing the stream functions associated with the vortex structure for each planar two-dimensional cross-sectional plane at a given z-value. The characteristic vortex size can then be estimated as the radial distance from the vortex centre where the velocity magnitude is zero to a vortex streamline associated with a stream function of a specified value. In this case, we choose $\phi = -1.009 \times 10^{-6}$ for convenience with a reference stream function $\phi = 0$ arbitrarily defined at $r = 2$ mm.

A comparison between the characteristic vortex dimensions from the experimental data of Fig. 6b and the

numerical simulation data of Fig. 6c is plotted in Fig. 9. We observe the strong qualitative correlation as well as the reasonable quantitative agreement despite the simplicity of the model employed. In both cases, the vortex strength, measured by the velocity magnitude shown in Fig. 6, and hence the characteristic vortex dimension, decreases towards the cavity floor where a stagnation point $\mathbf{U} = 0$ exists, representing a funnel-like vortex structure (Yeo et al. 2006a; Arifin et al. 2007). Strictly speaking, the stagnation point is a pseudo-fixed point (attractor or node) since the fluid must recirculate upwards through a central column, as shown in Fig. 7 due to a divergence-free condition ($\nabla \cdot \mathbf{U} = 0$) stipulated by flow conservation. Nevertheless, the fluid velocity $\mathbf{U}$, although non-zero, is small near the single fixed point, which can be converted into an attractor if a larger local force acts on a particle that opposes the vector direction of $\mathbf{U}$ (Batchelor 1951). If this occurs, as in the case of the blood plasma separation experiments in Arifin et al. (2007), particulate matter initially suspended in the fluid is trapped at this point.

The funnel-like shape of the helical vortex flow is characteristic of Batchelor flows (Batchelor 1951; Pao 1972) between a co-axial disk pair, the bottom disk held stationary and the top disk rotating at constant speed, as was speculatively alluded to in Yeo et al. (2006a) and Arifin et al. (2007). The decreasing velocity magnitude |$\mathbf{U}$| along the vertical z-direction towards the bottom of the chamber, as depicted in Figs. 6 and 9, results in decreasing centrifugal forces. Within the rotating core of the fluid, the inward radial pressure exerted by the boundaries balances the centrifugal force (Benton and Clark 1974). However, due to the no-slip boundary condition imposed by the stationary bottom of the cavity, a thin boundary layer in the fluid just above the cavity floor (known as the *Ekman layer*) exists wherein the centrifugal force is suppressed (Greenspan 1968). Consequently, an inward radial pressure gradient arises which generates an inward radial velocity, driving liquid to spiral towards the central core (Khomenko and Babiano 1999).

Figure 10 verifies the enhancement of the inward radial velocity in the Ekman layer. The parabolic radial velocity profile instead of one that monotonically increases

Fig. 8 a Lateral and **b** top views of the three-dimensional visualization of the flow field trace illustrating the downward spiral of the fluid along the sidewalls of the cavity and its return trajectory upwards via a central column as a consequence of the combined meridional and circumferential fluid motion
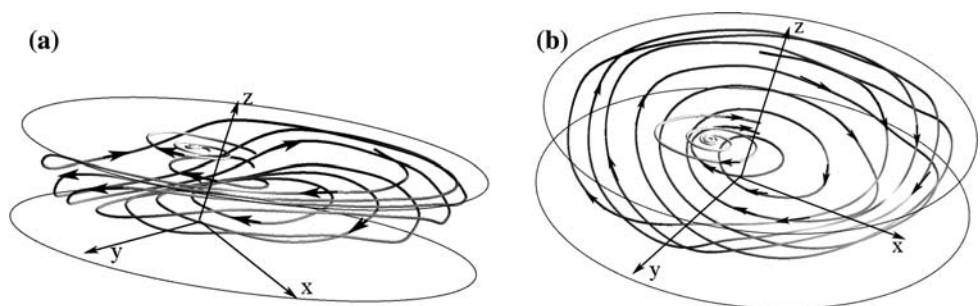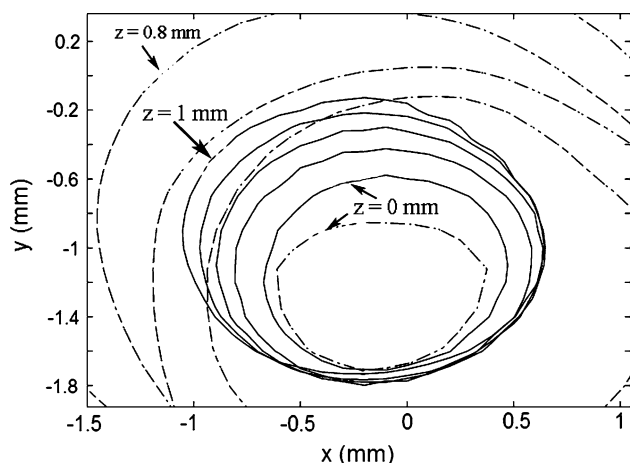
Fig. 9 Characteristic vortex dimensions from the numerical (*solid lines*) and experimental (*dashed lines*) results showing a decrease in vortex size towards the cavity floor, hence verifying the existence of a helical vortex structure. The asymmetry exhibited by the stream function contours again verifies the offset of the vortex from the vertical axis, which can be visualized in Figs. 6, 7, and 8
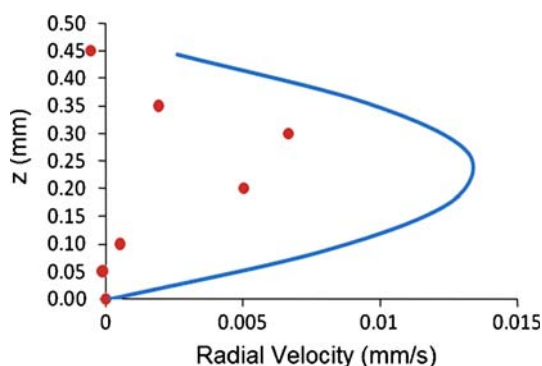

Fig. 10 Experimental (*dots*) and numerical (*line*) radial velocities at various depths in the cylindrical cavity, taken in the vicinity close to side wall at $r = 1.5$ mm. The increase in the inward radial velocity due to the suppression of the centrifugal force in the Ekman layer can be seen, as schematically illustrated in Fig. 3

confirms the suppression of the centrifugal forces due to the no-slip boundary condition. Outside the Ekman boundary layer, away from the cavity bottom, the radial velocity once again diminishes (Greenspan 1968). Figures 6, 7, 8, 9, and 10 confirm the helical flow-like behavior speculated in our earlier work (Yeo et al. 2006a; Arifin et al. 2007) with good qualitative and order of magnitude quantitative agreement between the experimental and numerical results.

4.2 Quantification of mixing intensity

To quantify the mixing action, we conducted a transient pixel intensity analysis of grayscale images of the dye during mixing due to the ionic wind-induced liquid

recirculation. Briefly, the still image frames at 0.2 s intervals were extracted from the high speed video file. Each image was 320×240 pixels wide, whose width spanned the cavity diameter; each pixel therefore captured a 12.5 μm $\times$ 12.5 μm area of the flow field. Each successive image was subsequently rendered into a grayscale images using Photoshop® (Adobe®, San Jose, CA) and a simple script written in MATLAB® (MathWorks™, Natick, MA) to determine its pixel intensity distribution. The logarithmic standard deviation of the pixel intensities, normalized by the initial standard deviation, is plotted with respect to time in Fig. 11 for a fixed applied frequency (70 kHz) and different applied voltages. In the case of a purely diffusive mechanism where the concentration throughout the liquid is anticipated to homogenize exponentially over time, the diffusivity D, a measure of the mixing intensity, can be estimated from a linear regression of Fig. 11a (Wang et al. 2004). In other words, the slope of the curves in Fig. 11a is proportional to D/L^2, where L is the characteristic length scale of the system, taken to be the diameter of the cavity, typically on the order of 10^{-3} m. When no electric field is applied, it can be determined from Fig. 11a that the slope is approximately -10^{-3}, giving a diffusivity D_0 of 10^{-9} m^2/s, which is consistent with typical diffusive coefficient values in a situation where mixing is solely dependent on diffusion. With applied electric fields, however, we observe an increase in the values of the slope and hence the effective diffusivity D_{eff} with an increase in the voltage, which is a consequence of convective mixing induced by the liquid recirculation.

The ratio D_{eff}/D_0 then reveals the extent of mixing enhancement by the convective flow relative to simple diffusion. For the 70 kHz data plotted in Fig. 11a, the mixing intensity is enhanced by up to two orders of magnitude at the highest applied voltage. The same trend is also observed at frequencies below 70 kHz. The effect of frequency is most clearly shown in Fig. 11b, where the logarithmic values of the applied field $E \sim V/L$ is plotted against the ratio D_{eff}/D_0. The inset of Fig. 11b shows the slopes of the data of $\log E$ against $\log(D_{eff}/D_0)$ at different frequencies, indicating the exponent n with respect to E by which the mixing diffusivity scales to at different frequencies, i.e., $(D_{eff}/D_0) \sim E^n$. It must be acknowledged that the reliability of the data is poor at lower frequencies (10 kHz), and especially at low voltages that are close to the threshold voltage for which the flow can exist at the given frequency, since the ionic-wind driven flow cannot be consistently maintained (see Fig. 12). However, at high frequencies we observe an almost quintical scale (to the fifth order) of the mixing diffusivity with respect to field strength, much more than the quadratic field dependence obtained for nonlinear electrokinetic devices (Wang et al. 2004). It should be noted, however, that the two-dimensional pixel intensity
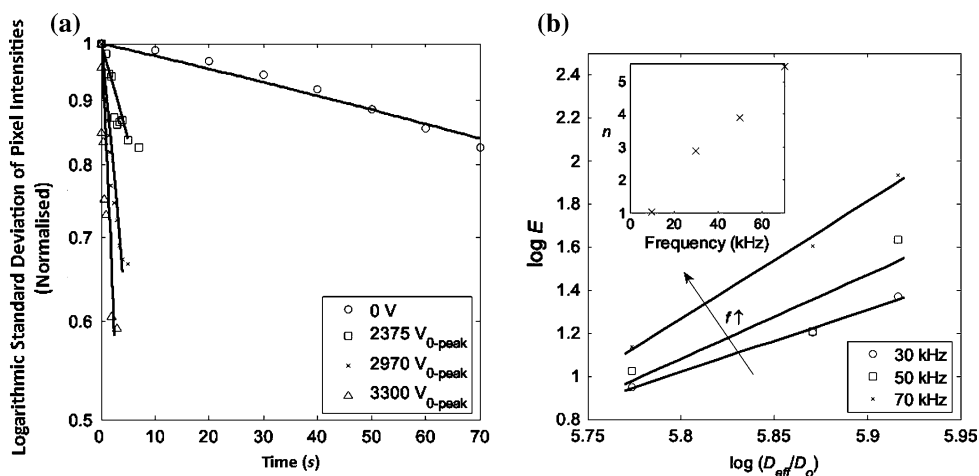
Fig. 11 Convective enhancement of the mixing intensity through surface vortex generation. **a** Normalised standard deviation in the pixel intensity as a function of time for various applied voltages. The applied frequency is fixed at 70 kHz for the data shown. **b** Effect of the electric field E on the mixing intensity, as measured by the ratio

between the effective diffusivity D_{eff} and the diffusivity in the absence of flow D_0, for various frequencies. The inset shows the variation in the exponent n representing the slope of the log E against $\log(D_{\text{eff}}/D_0)$ data with the applied frequency. All lines are least square fit to the data shown
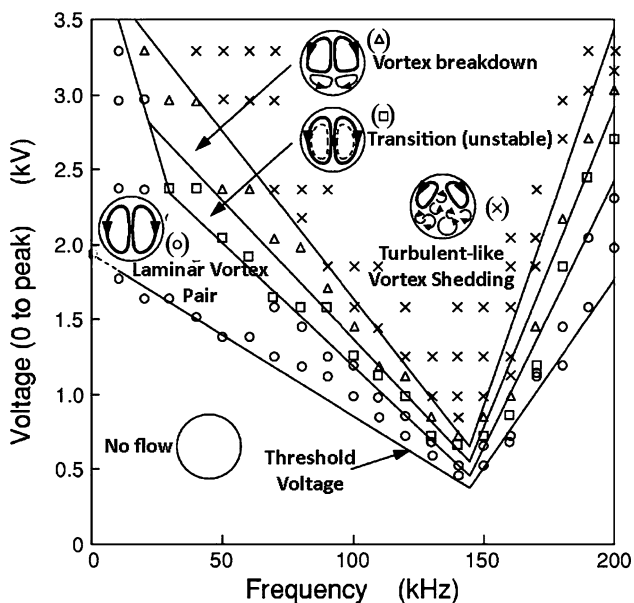

Fig. 12 Flow recirculation behavior as a function of applied frequency and applied voltage for the electrode configuration shown in Fig. 2b. The various symbols are experimental points that indicate the different flow behavior observed (Yeo et al. 2006b)

analysis can only approximate the mixing diffusivities as it is independent of the chamber depth. Nevertheless, the secondary bulk recirculation traversing the whole liquid body, as shown in Fig. 8 is expected to further promote the mixing action.

It has been observed that high voltages and high frequencies give rise to enhanced mixing, which can best be explained by the mapping of the recirculation patterns to various frequencies and voltages, as illustrated in Fig. 12.

At frequencies below the optimum value at approximately 145 kHz (left half of the map), the primary vortices become unstable as the voltage is increased and eventually break down to give rise to secondary subvortices (Fig. 13). For the small Reynolds number encountered here, this Taylor–Couette-like behavior of the vortices is intriguing. Such successive breakdown in the vortices then gives rise to a cascade of vortex sizes over a continuum of length scales, which, in turn, results in enhanced mixing (Yeo et al. 2006b). More work is currently being undertaken to further quantify and elucidate the physical mechanism responsible for this chaotic behavior, especially in the highly unstable region where vortex breakdown occurs. In any case, this very intense mixing provides a suitable mechanism to overcome the mixing deficiencies that typically plague microfluidic devices without the need for complex fabrication procedures associated with conventional micromixers.

5 Conclusion

MicroPIV studies have been carried out to characterize the three-dimensional flow field arising due to ionic wind-induced microcentrifugation in a small cylindrical cavity. This study represents the first attempt to visualize the flow field since the authors' recent discovery of the phenomenon in order to confirm the speculated mechanism that gives rise to the vortical flow behavior. This is complimented by numerical simulations of the fluid flow within the cavity driven by a rotational boundary condition imposed at the liquid surface obtained from the experimental data. A comparison between the experimental and numerical
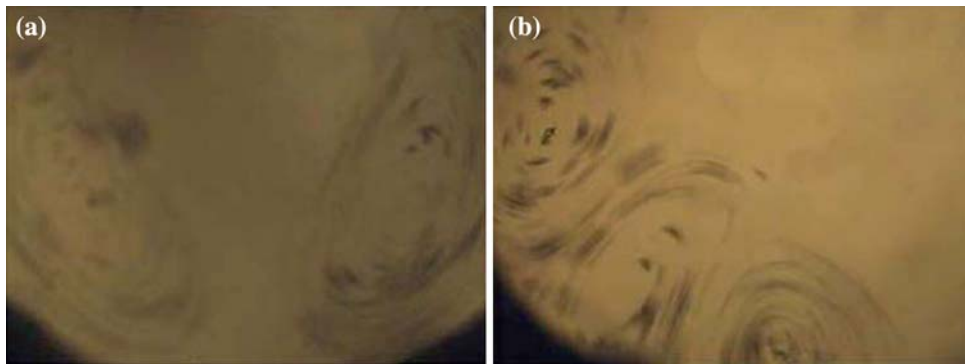
Fig. 13 Particle-aided flow visualization illustrating **a** the primary vortices observed in the laminar vortex pair regime delineated by the flow pattern map in Fig. 12 and **b** the breakdown of a primary vortex into secondary subvortices when the voltage is increased beyond a threshold value such that the flow moves into the vortex breakdown region in Fig. 12. The vigorous secondary subvortices result in enhanced mixing intensities

results shows good qualitative agreement and modest quantitative estimates despite the simplicity of the numerical model. Several salient features of the flow field were observed in previous work, such as the tapering vortical structure (reduction in the velocity magnitude and hence the vortical strength and characteristic vortex dimension), the enhanced inward radial velocity in the Ekman layer in the fluid immediately adjacent to the cavity floor, the recirculation of the fluid up a central column, and the agreement in the order of magnitude velocity estimates. The results, which were able to capture these salient features, serve to verify the speculated model.

In addition, we also attempted to formally quantify the ability of the technique to drive micromixing which was only qualitatively demonstrated previously. Through a pixel intensity analysis of images captured through high speed video microscopy as the mixing progresses, we were able to quantify the mixing intensity in terms of an effective diffusivity as a function of the applied voltage and AC frequency relative to pure diffusive mixing. Our results show a significant intensification in the mixing intensity using the electrohydrodynamically driven microcentrifugal flow by almost two orders of magnitude, at least based on two-dimensional azimuthal surface recirculation alone. The transition to enhanced mixing is associated with the sequential breakdown in the vortices due to various instabilities, forming the focus of our future work.

References

Arifin D, Yeo L, Friend J (2007) Microfluidic blood plasma separation via bulk electrohydrodynamic flows. Biomicrofluidics 1:014103

Batchelor G (1951) Note on a class of solutions of the Navier–Stokes equations representing steady rotationally-symmetric flow. Q J Mech Appl Math 4:29–41

Benton E, Clark A (1974) Spin-up. Annu Rev Fluid Mech 6:257–280

Chen C, Santiago J (2002) A planar electroosmotic micropump. J Micromech Microeng 11:672–683

Ducree J (2008) Centrifugal microfluidics. In: Li D (ed) Encyclopedia of microfluidics and nanofluidics. Springer, New York

Greenspan H (1968) The theory of rotating fluids. Cambridge Univeristy Press, Cambridge

Guigan J (1998) Method and apparatus for obtaining and delivering a predetermined quantity of plasma from a blood sample for analysis purpose. U.S. Patent No. 4788154

Haeberle S, Brenner T, Zengerle R, Ducree J (2006) Centrifugal extraction of plasma from whole blood on a rotating disk. Lab Chip 6:776–881

Hutchinson B, Raithby G (1986) A multigrid method based on the additive correction strategy. Numer Heat Transf 9:511–537

Kawamoto H, Umezu S (2005) Electrohydrodynamic deformation of water surface in a metal pin to water plate corona discharge system. J Phys D 38:887–894

Khomenko G, Babiano A (1999) Quasi-three-dimensional flow above the Ekman layer. Phys Rev Lett 83:84–87

Kinoshita H, Kaneda S (2007) Three-dimensional measurement and visualization of internal flow of a moving droplet using confocal micro-PIV. Lab Chip 7:338–346

Laser D, Santiago G (2004) A review of micropumps. J Micromech Microeng 14:35–64

Li D (2004) Electrokinetics in microfluidics. Academic Press, London

Loeb L (1965) Electrical corona. University of California Press, Berkeley

Madou M, Zoval J, Jia G, Kido H, Kim J, Kim N (2006) Lab on a CD. Annu Rev Biomed Eng 8:601–628

Nguyen N, Wereley S (2006) Fundamentals and applications of microfluidics, 2nd edn. Artech House, Boston

Ohyama RI, Kaneko K, Chang JS (2003) Flow visualisation and image analysis of gas-phase ac corona discharge induced electrohydrodynamic liquid flow in a stratified fluid. IEEE Trans Dielectr Elec Ins 10:57–64

Pao HP (1972) Numerical solution of the Navier–Stokes equations for flows in the disk-cylinder system. Phys Fluids 15:4–11

Papautsky I, Asgar A, Bhagat S (2008) Microscle flow visualization. In: Li D (ed) Encyclopedia of microfluidics and nanofluidics. Springer, New York

Pugia M, Profitt J, Schulman L (2004) Method and apparatus for separation of particles in a microfluidic device. W.O. Patent No. 2004/061413

Raghavan R, Friend J, Yeo L (2009) Particle concentration via acoustically-driven microcentrifugation: microPIV flow visualisation and numerical modelling studies. Microfluid Nanofluid. doi:10.1007/s10404-009-0452-3

Raw M (1996) Robustness of coupled algebraic multigrid for the Navier–Stokes equations. AIAA Technical Paper 96-0297 (American Institute of Aeronautics and Astronautics, Reston, VA, USA)

Shelby J, Lim D, Kuo J, Chiu D (2003) Microfluidic systems: high radial acceleration in microvortices. Nature 425:38

Tan M, Friend J, Yeo L (2007) Surface acoustic wave driven microchannel flow. In: Proceedings of the 16th Australasian Fluid Mechanics Conference, Gold Coast, QLD, Australia, pp 790–793

Wang P, Chen Z, Chang HC (2006) A new electro-osmotic pump based on silica monoliths. Sens Actuators B 113:500–509

Wang SC, Lai YW, Ben Y, Chang HC (2004) Microfluidic mixing by dc and ac nonlinear electrokinetic vortex flows. Ind Eng Chem Res 43:2902–2911

Yeo L, Friend J (2009) Ultrafast microfluidics using surface acoustic waves. Biomicrofluidics 3:012002

Yeo L, Friend J, Arifin D (2006a) Electric tempest in a teacup: the tea leaf analogy to microfluidic blood plasma separation. Appl Phys Lett 89:103516

Yeo L, Hou D, Maheshswari S, Chang HC (2006b) Electrohydrodynamic surface microvortices for mixing and particle trapping. Appl Phys Lett 88:233512